THE UNIVERSITY *of* EDINBURGH

Edinburgh Research Explorer

Magnetic vortex effects on first-order reversal curve (FORC) diagrams for greigite dispersions

OPEN ACCESS

Magnetic vortex effects on first-order reversal curve (FORC) diagrams for greigite dispersions

Miguel A. Valdez-Grijalva [a,b,*], Adrian R. Muxworthy [a], Wyn Williams [c],
Pádraig Ó Conbhuí [c], Lesleis Nagy [e], Andrew P. Roberts [d,f], David Heslop [d,f]

[a] *Department of Earth Science and Engineering, Imperial College London, SW7 2BP, UK*
[b] *Instituto Mexicano del Petróleo, 07730, Mexico*
[c] *School of GeoSciences, University of Edinburgh, EH9 3FE, UK*
[d] *Research School of Earth Sciences, Australian National University, ACT 2601, Australia*
[e] *Scripps Institution of Oceanography, 9500 Gilman Drive, La Jolla, CA 92093, United States of America*
[f] *Research Institute of Geology and Geoinformation, Geological Survey of Japan, National Institute of Advanced Industrial Science and Technology, 305-8567, Japan*

ARTICLE INFO

ABSTRACT

First-order reversal curve (FORC) diagrams are used increasingly in geophysics for magnetic domain state identification. The domain state of a magnetic particle is highly sensitive to particle size, about which FORC diagrams provide valuable information. However, the FORC signal of particles with nonuniform magnetisations, which are the main carrier of natural remanent magnetisations in many systems, is still poorly understood. In this study, the properties of non-interacting, randomly oriented dispersions of greigite (Fe_3S_4) in the uniform single-domain (SD) to non-uniform single-vortex (SV) size range are investigated via micromagnetic calculations. Signals for SD particles (<50 nm) are found to be in excellent agreement with previous SD coherent-rotation studies. A transitional range from $\sim$50 nm to $\sim$80 nm is identified for which a mixture of SD and SV behaviour produces complex FORC diagrams. Particles $>\sim$80 nm have purely SV behaviour with the remanent state for all particles in the ensemble in the SV state. It is found that for SV ensembles the FORC diagram provides a map of vortex nucleation and annihilation fields and that the FORC distribution peak should not be interpreted as the coercivity of the sample, but as a vortex annihilation field on the path to saturation.

1. Introduction

First-order reversal curve (FORC) diagrams are a powerful tool in rock magnetic studies, which allow mineral and domain state identification as well as quantification of magnetostatic interactions among particles (Pike et al., 1999; Roberts et al., 2000, 2014; Dumas et al., 2007; Egli et al., 2010). As such, they have been the subject of numerical studies aimed at relating the behaviour of individual magnetic particles and small assemblages to experimental bulk properties (Pike et al., 1999; Pike and Fernandez, 1999; Carvallo et al., 2003, 2006; Muxworthy et al., 2004; Muxworthy and Williams, 2005; Newell, 2005; Harrison and Lascu, 2014; Valdez-Grijalva and Muxworthy, 2018; Roberts et al., 2017).

With the exceptions of Pike and Fernandez (1999), Carvallo et al. (2003) and Roberts et al. (2017), all of these numerical studies have concentrated on FORC diagrams for ideal, uniformly magne-

tised single-domain (SD) particles. They have shown that uniaxial SD particles produce patterns in FORC diagrams (Muxworthy et al., 2004; Newell, 2005; Harrison and Lascu, 2014) that are distinct from those for SD materials with cubic anisotropy (Muxworthy et al., 2004; Harrison and Lascu, 2014; Valdez-Grijalva and Muxworthy, 2018). However, it is well-documented that most natural systems have magnetic signals dominated by larger grains with more complex magnetic domain states (Dunlop and Özdemir, 1997; Roberts et al., 2017). Grains just above the SD threshold size (e.g., $\sim$64 nm for equidimensional magnetite, $\sim$54 nm for greigite), are typically in a single-vortex (SV) state. The SV state dominates magnetic structures over an order of magnitude of size variations (Nagy et al., 2017; Valdez-Grijalva et al., 2018), which is much wider than the stable SD size range. SV grains have recently been found to be geologically meta-stable and retain relatively high remanences (Almeida et al., 2014; Nagy et al., 2017; Valdez-Grijalva et al., 2018).

Experimental studies on nano-patterned arrays of SV particles (Pike and Fernandez, 1999; Dumas et al., 2007) found that FORC diagrams are significantly more complex than for SD signals,

with complex off-axis patterns that are related to vortex nucleation/annihilation processes. However, it is difficult to relate the behaviour of 2D nano-patterned arrays to the behaviour of natural particle systems found in geological samples. In natural samples, particles with varying size and orientation are dispersed in 3 dimensions. Thus, it is important to understand the contribution of dispersions of randomly aligned SV particles to FORC diagrams. Numerical modelling can aid the study of such systems. Carvallo et al. (2003) used a finite-difference model to calculate FORC distributions for SV magnetite particles; however, that study primarily examined the effects of interactions within small clusters of cubic grains, and neither random particle distributions nor realistic grain morphologies were included.

In this study, we employ a micromagnetic finite element method (FEM) to obtain FORC diagrams for non-interacting ensembles of SD and SV greigite (Fe_3S_4). Greigite is the iron-sulphide counterpart to magnetite. Recent interest in greigite comes from both its promising properties for material science (Li et al., 2014) and the abundance of this mineral in sedimentary rocks for Earth science (Roberts et al., 2011). FORC diagrams are often used to help identify greigite. The relatively high anisotropy of greigite means that the behaviour of this mineral is representative of cubic-anisotropic ferri- and ferro-magnets like magnetite and iron. We calculate FORC diagrams for simulations of non-interacting dispersions of randomly oriented greigite with sizes 30–100 nm; this size range covers the SD–SV threshold (Valdez-Grijalva et al., 2018). Simulations were carried out for an ensemble of 500 particles with random orientations. The unstructured discretisation of FEMs allows us to simulate realistic greigite particle shapes as observed in nature. We determine the onset of SV behaviour and its consequences for FORC diagram interpretation.

2. Methods

2.1. The micromagnetic algorithm

A ferromagnetic material—neglecting thermal and magnetostrictive effects—has a Gibbs free-energy functional given by (Brown, 1963):

$$E_G = \int_{\Omega} (\phi_{\text{exchange}} + \phi_{\text{anisotropy}} + \phi_{\text{stray}} + \phi_{\text{external}}) \, d^3 \boldsymbol{r}, \qquad (1)$$

where Ω is the ferromagnetic volume. Here,

$$\phi_{\text{exchange}} = A|\nabla \boldsymbol{m}|^2, \qquad (2)$$

where $\boldsymbol{m}$ is the reduced magnetisation vector and A the exchange stiffness constant, provides an expression for the energy density due to quantum-mechanical exchange forces (Landau and Lifshitz, 1935).

$$\phi_{\text{anisotropy}} = \frac{K_1}{2} \sum_{i \neq j} \gamma_i^2 \gamma_j^2 + K_2 \prod_i \gamma_i^2, \qquad (3)$$

where γ_i represent the direction cosines and K_1 and K_2 the first and second magnetocrystalline anisotropy (MCA) constants, is the MCA energy density in the cubic anisotropy system. In terms of the reduced magnetisation vector components, this becomes:

$$\phi_{\text{anisotropy}} = K_1(m_x^2 m_y^2 + m_y^2 m_z^2 + m_z^2 m_x^2), \qquad (4)$$

where K_2 is neglected because K_1 is the dominant term at room temperature. The magnetostatic self-energy density is given by:

$$\phi_{\text{stray}} = -\frac{\mu_0 M_S}{2} \boldsymbol{m} \cdot \boldsymbol{H}_{\text{stray}}, \qquad (5)$$

where $\boldsymbol{H}_{\text{stray}}$ is the stray field produced by the ferromagnetic body and M_S is the saturation magnetisation. Finally, the energy density due to an external magnetic field $\boldsymbol{H}_{\text{external}}$ is:

$$\phi_{\text{external}} = -\mu_0 M_S \boldsymbol{m} \cdot \boldsymbol{H}_{\text{external}}. \qquad (6)$$

Such magnetic particle systems will be driven spontaneously toward an equilibrium state with a locally minimal magnetic Gibbs free-energy (Brown, 1963). In this study we utilise a modified gradient descent method to find the equilibrium magnetisation (Ó Conbhuí et al., 2018).

Discretisation of the spatial domain is achieved by decomposing the volume into tetrahedral elements. This allows modelling of particles with arbitrary geometries. To model accurately nonuniform magnetisations, spatial discretisation in the model should be smaller than the exchange length $l_{\text{exch.}} = \sqrt{2A/\mu_0 M_S^2}$ (Rave et al., 1998), which for greigite is $l_{\text{exch.}} \approx 6.6$ nm; a maximum element size of 5 nm was used for all simulations. The non-local problem of calculating the stray field is resolved by a hybrid finite-element/boundary-element method (BEM) formulation (Fredkin and Koehler, 1990).

The fundamental magnetic parameters of greigite used throughout this investigation are the saturation magnetisation $M_S = 3.51 \mu_B$ per cell unit (p.c.u.) (Li et al., 2014) or $\sim 2.7 \times 10^5$ A/m which is $\sim 11\%$ higher than the value previously reported by Chang et al. (2009) of $3.25 \mu_B$ p.c.u. (and $\sim 57\%$ the value of M_S for magnetite). Winklhofer et al. (2014) used ferromagnetic resonance spectroscopy to estimate the anisotropy constants. They obtained a (first) cubic MCA constant $K_1 = -1.7 \times 10^4$ J/m^3 and negligible second MCA constant K_2 to K_1 ratio, i.e., the easy axes are the $\langle 111 \rangle$ directions. The data are also consistent, with a positive K_1 value and large $K_2 \approx 3K_1$ and, thus, with $\langle 100 \rangle$ easy axes; however, there is indirect (Winklhofer et al., 2014) and direct (Li et al., 2014) evidence favouring the anisotropy model with negative K_1 that we use throughout this work.

The exchange stiffness constant was estimated by Chang et al. (2008) to be $A = 2 \times 10^{-12}$ J/m. The exchange energy in a ferrimagnet is related to the spin wave stiffness. Spin waves are collective wave-like disturbances in the magnetic ordering of magnetic matter. Experimental observation of spin waves can be achieved by several methods, e.g., inelastic neutron scattering and spin wave resonance. These experimental techniques require, however, relatively large, uniform crystals on which to observe spin wave propagation. Fabrication of such samples is as yet impossible for greigite, so Chang et al. (2008) measured the saturation magnetisation (in a field of 5 T) of powdered greigite samples at low temperatures. Using the spin wave expansion of the spontaneous magnetisation for low temperatures $M(T) = M_S(1 - CT^{3/2})$ (Bloch, 1932), where C is a function of the spin wave stiffness, they were able to fit the data and obtain an estimate of the spin wave stiffness and, therefore, the exchange stiffness constant. Determination of the spin wave stiffness through different approaches like inelastic neutron scattering (Torrie, 1967), low-temperature heat capacity (Kenan et al., 1963), and low-temperature M_S measurements (Aragón, 1992), however, has been known to produce variable results for magnetite (Chang et al., 2008). This places a degree of uncertainty on this measurement for greigite that is difficult to quantify in the absence of measurements acquired through means other than low-temperature saturation magnetisation.

Chemical alteration at high temperatures has made it difficult to measure accurately the Curie temperature greigite; however, there is strong evidence for a Curie temperature $T_C > 620$ K (Roberts et al., 2011). The exchange energy is directly related to T_C; within a mean field approximation (Kouvel, 1956):

$$T_C = \frac{4\sqrt{2} J_{AB}}{K_B} \sqrt{S_A S_B (S_A + 1)(S_B + 1)}, \qquad (7)$$

where K_B is Boltzmann's constant, J_{AB} is the exchange integral between the A- and B-sites of the inverse spinel crystal lattice of greigite and S_A, S_B the spin magnetic moments of A- and B-sites, respectively. Inserting the relatively low value of $J_{AB} \approx 1$ meV measured by Chang et al. (2008) and $S_A = 1.54$, $S_A = 1.63$ (Chang et al., 2009) predicts a low $T_C \approx 260–287$ K. This suggests that there is significant uncertainty in the determination of A by Chang et al. (2008). A value of $J_{AB} = 2.31$ meV results in a $T_C \approx 620$ K. However, mean field approximations can overestimate the Curie temperature, so the value of the exchange integral J_{AB} could be larger than this and be consistent with experimental bounds.

Increased A values have the effect of increasing domain wall widths and, thus, the critical size d_0 of the transition from uniform to non-uniform magnetisation. To quantify this effect, a calculation in the manner of Valdez-Grijalva et al. (2018) of the SD to SV critical size d_0 was made for A values of 4×10^{-12} J/m and 8×10^{-12} J/m, which produce d_0 increases from $d_0 \approx 54$ nm (Valdez-Grijalva et al., 2018) (for the value reported by Chang et al., 2008) to $d_0 \approx 62$ nm and $d_0 \approx 90$ nm, respectively. Changes in the exchange stiffness constant have little effect on the coercivities of SD particles because the energy of an ideal point-dipole particle only depends on M_S and K_1 (Valdez-Grijalva and Muxworthy, 2018); it is plausible then that SV grain coercivities are similarly unaffected or only slightly affected by changes in the exchange stiffness constant, especially if vortices retain their overall structure during the switchings responsible for bulk coercivities. Thus, uncertainty in the value of A produces uncertainty in the sizes for which particles should transition from one domain state to another, but probably not in the coercivities. In the absence of improved measurements of A, the value determined by Chang et al. (2008) is used throughout this work.

2.2. The FORC model

FORC diagrams are constructed from a class of partial hysteresis curves called first-order reversal curves (Mayergoyz, 1986) that each start at an applied field value B_a along the main hysteresis branch and trace the magnetisation as the field B_b is increased to saturation. A magnetisation function on two variables $M = M(B_a, B_b)$ is thus obtained. The FORC distribution ρ is then defined as (Roberts et al., 2000):

$$\rho = -\frac{1}{2}\frac{\partial^2 M}{\partial H_a \partial H_b} = -\frac{\mu_0^2}{2}\frac{\partial^2 M}{\partial B_a \partial B_b}, \tag{8}$$

where μ_0 is the magnetic constant (or vacuum permeability) and $H = B/\mu_0$.

Once $M(B_a, B_b)$ is obtained, calculation of $\rho(B_a, B_b)$ is done by least-squares fitting of a degree 2 polynomial surface $a_0 + a_1 B_a + a_2 B_b + a_3 B_a B_b + a_4 B_a^2 + a_5 B_b^2 + \text{error} = M(B_a, B_b)$ on a subgrid of $M(B_a, B_b)$ centred around (B_a, B_b) as determined by the so-called smoothing factor (SF) and including $(2 \times \text{SF} + 1)^2$ points; the value of ρ is then simply $-\mu_0^2 a_3/2$ (Pike et al., 1999). FORC diagrams are usually presented with rotated axes $B_c = (B_b - B_a)/2$, $B_u = (B_b + B_a)/2$.

Distributions with random orientations of magnetic particles with respect to the applied field were determined by taking 500 field orientations from a sector of the unit sphere (Fig. 1). We use 500 field orientations as a workable compromise between accuracy and calculation speed. Also, for each particle/field-orientation, the hysteresis curve consists mostly of reversible motion of the magnetisation; thus, we only need to calculate the main branch of the hysteresis loop and the few reversal curves starting at the different switching fields along the main branch (Valdez-Grijalva and Muxworthy, 2018). These simplifications reduce vastly the number of calculations needed without loss of important information. The
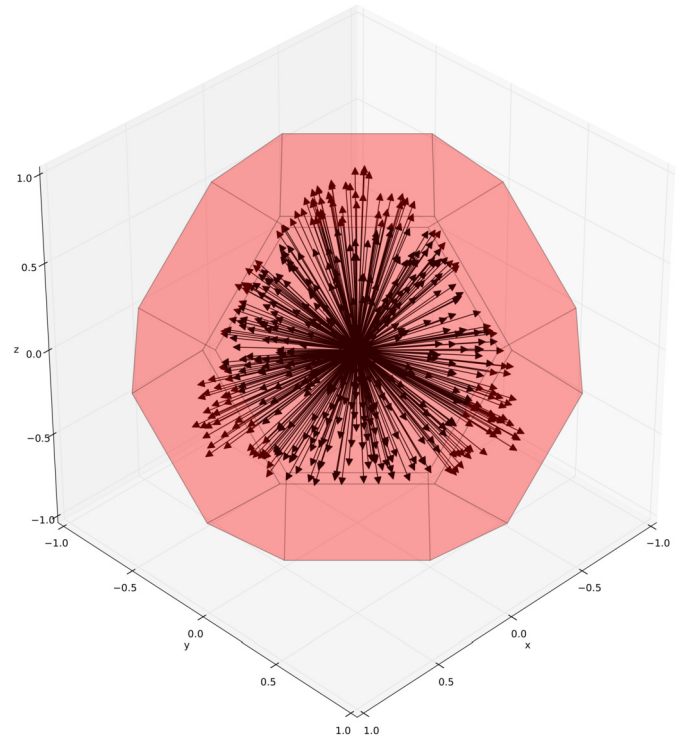
Fig. 1. Model geometry and field orientations. The most common morphology for authigenic greigite is truncated octahedral. To avoid the high density of field orientations necessary near the sphere poles when using a regular grid, 500 random field orientations (arrows) were chosen from a uniform distribution over a sector of the unit sphere. The periodicity of the magnetocrystalline anisotropy and particle symmetry allow modelling of the effects of field orientations on only a sector of the sphere without loss of generality.

external-field rate of change for all models was 1 mT with a saturation field of 250 mT, so that 501 reversal curves were calculated for each particle/field-orientation.

Scanning electron and transmission electron micrographs of naturally occurring greigite samples (Snowball, 1997; Vasiliev et al., 2008; Roberts, 2015) reveal that greigite tends to grow authigenically as well-defined regular truncated octahedral particles. Micromagnetic calculations for truncated octahedral greigite particles indicate that the SD–SV threshold occurs at ~54 nm (Valdez-Grijalva et al., 2018). In this study we model FORC diagrams for non-interacting ensembles of truncated octahedral greigite particles sized 30–100 nm (where size is normalised to the volume of a cube) at 2 nm size intervals. This range is chosen because it spans the zero-field transition from SD to SV behaviour.

3. Results

For ensembles with SD particles < 50 nm, hysteresis behaviour is dominated by coherent rotation (Fig. 2). This is seen by comparing FORC diagrams for these ensembles (Fig. 2b) with those of idealised SD (effectively a single magnetic dipole), coherently rotating greigite particles (Fig. 2a) determined using the method outlined by Valdez-Grijalva and Muxworthy (2018). Diagrams for particles < 50 nm obtained with the micromagnetic algorithm (Fig. 2b) are offset ~3 mT to the left compared to the dipole model (Fig. 2a); lower coercivities due to the micromagnetic algorithm, which includes flowering (small deviations from a perfect SD structure) as a result of magnetostatic self-interaction effects, account for this effect.

Particles with cubic anisotropy have hysteresis behaviour that departs from that seen in the simple hysteron with one plus and one minus magnetisation states. There exist intermediate easy axis
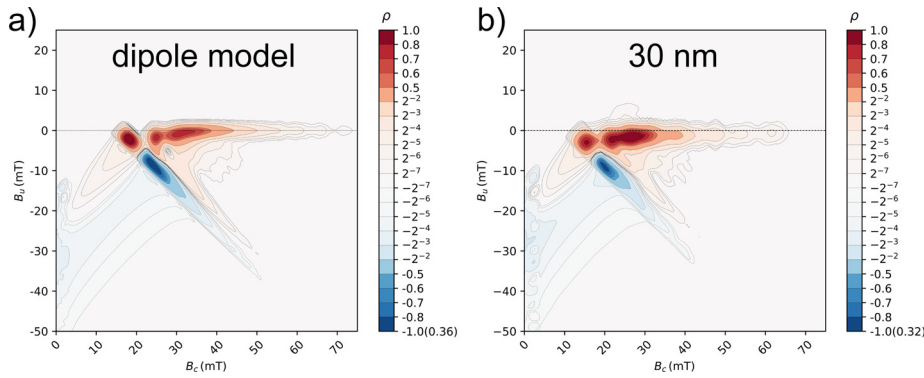
Fig. 2. Comparison between FORC diagrams produced with dipole and micromagnetic models. a) Dipole model; FORC diagram (SF = 4) for a non-interacting ensemble of idealised (size-independent) SD greigite particles obtained using the model of Valdez-Grijalva and Muxworthy (2018). b) Micromagnetic model; FORC diagram (SF = 4) for a non-interacting ensemble of 30 nm truncated octahedral greigite particles. Up to 48 nm, the FORC diagram is that of an ensemble of coherently rotating SD moments. For particles larger than 48 nm, magnetic vortex effects become important. Dashed contour lines denote negative ρ values. Negative contour values are scaled by the number in brackets at the bottom of the colour-bar legend. (For interpretation of the colours in the figure(s), the reader is referred to the web version of this article.)

states along hysteresis curves for the SD state (Valdez-Grijalva and Muxworthy, 2018). The tilted, elongated, negative-valued ridge (Fig. 2) is a consequence of the cubic anisotropy and is produced by the fraction of particles with a hard axis aligned closely with the applied field. These particles have the lowest switching fields: from the plus-state to an intermediate state at $B = B_*^+$ and from the intermediate state to the minus-state at $B = B_*^-$. Reversal curves with $B_*^- < B_a < B_*^+$ experience a sharp upward discontinuity at $B_b = B_+^* < |B_*^+|$ when hard-aligned particles return to the plus-state from their intermediate states. The combination of this type of irreversible event in hard-aligned particles causes the local peak at $B_c \approx 15$ mT, $B_u \approx -3$ mT (Fig. 2b). For reversal curves with $B_a < B_*^-$, hard-aligned particles are initially in the minus-state and undergo irreversible rotation to an intermediate state on the path to positive saturation at $B = B_*^- = |B_*^+|$ due to the symmetry of the particles and the lack of magnetostatic interactions. The combination of these irreversible events causes a negative FORC distribution response at $B_a = B_-^*$, $B_b = B_+^*$. The sum effect of this type of response for many particles with a distribution of switching fields produces the elongated negative contribution observed in all SD ensembles.

The fraction of particles with easy axis alignment close to the applied field orientation exhibits hysteron-like behaviour, i.e., just two switching fields: from the plus-state to the minus-state B_-^+ and *vice versa* B_+^-. The lack of interactions and the symmetry of particles in our simulations ensure that $|B_-^+| = B_+^-$. Thus, this fraction of particles produces FORC distribution responses at $B_a = B_-^+$, $B_b = B_+^-$. These types of irreversible responses accumulate on the line $B_a = -B_b$; they account for the most drastic changes in the magnetisation of the ensemble and, thus, account for the high slopes around the coercive field of the sample. This makes the position of the FORC diagram peak coincide with the coercivity of $B_C \approx 24$ mT for SD ensembles.

Particles with size $d \geq 50$ nm switch incoherently (Fig. 3); that is, the FORC diagrams depart from coherent rotation behaviour associated with SD particles as the tight boomerang-shaped FORC diagram pattern exhibited by the SD greigite (Fig. 2) becomes more fragmented (Fig. 4). This change is driven initially by particles with hard axes close to the applied field nucleating hard-aligned vortices as intermediate meta-stable states during hysteresis. Even though nucleation of hard-aligned vortices occurs in particles below the zero-field SD–SV threshold $d_0 \approx 54$ nm (Valdez-Grijalva et al., 2018), this is expected because vortex nucleation greatly reduces the magnetic free-energy. A corollary of this is that a fraction of particles (with easy axis alignment close to the applied field) above the zero-field SD–SV threshold can remain in a SD state
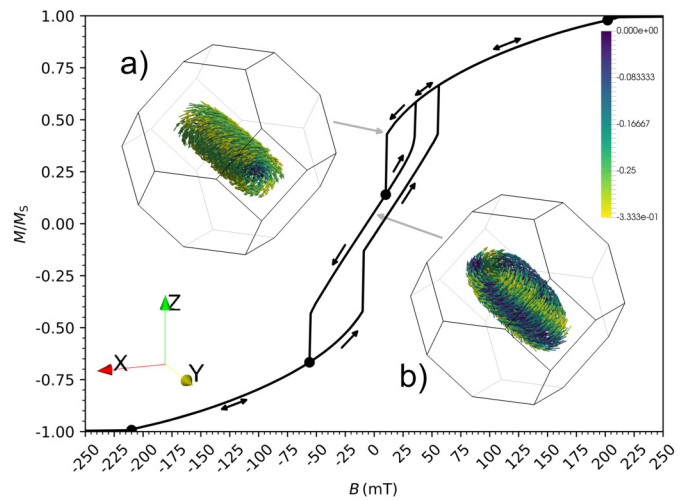

Fig. 3. Hysteresis and reversal curves for a 100 nm particle with hard axis close to the applied field. A hard-aligned vortex (a) is nucleated at ~200 mT. As the field decreases the vortex winds, which decreases its net magnetisation. At 10 mT the vortex switches to an easy axis alignment (the remanent state) (b). Calculation of the subset of reversal curves starting at the different switching fields (black dots) is sufficient to obtain the complete set of curves. Colours code for low anisotropy (yellow) to high anisotropy (indigo).

throughout hysteresis. These effects are due to distortion of the zero-field energy landscape by the applied field.

An appreciable positive source in the FORC distribution appears along the $B_u = 0$ axis at $B_c \approx 52$ mT (the B_c axis should not be confused with the coercivity B_C) for ensembles with particles ≥ 50 nm (Fig. 4); this contribution represents the annihilation of vortex states on the return to positive saturation. The elongated, negative ridge due to SD particles with cubic MCA and its corresponding symmetric positive response move to lower (B_c, B_u) values (Fig. 4a) and the first responses for $B_u > 0$ begin to form (Fig. 4a); these are elongated features at 45° to the $B_u = 0$ axis, which are different to the vertical widening usually attributed to magnetostatic interactions (Pike et al., 1999; Muxworthy et al., 2004; Muxworthy and Williams, 2005).

For particles slightly below and above the SD–SV threshold d_0, vortex nucleation occurs only for negative applied field values, thus noticeable changes are not evident in FORC diagrams (Fig. 4a, b) or in the saturation remanence M_{RS} to saturation magnetisation M_S ratio up to 74 nm, whereas coercivity decreases sharply above 48 nm (Fig. 5b). The monotonically-decreasing coercivity trend is preserved up to 62 nm when it rises from $B_C \approx 16$ mT to ~20 mT
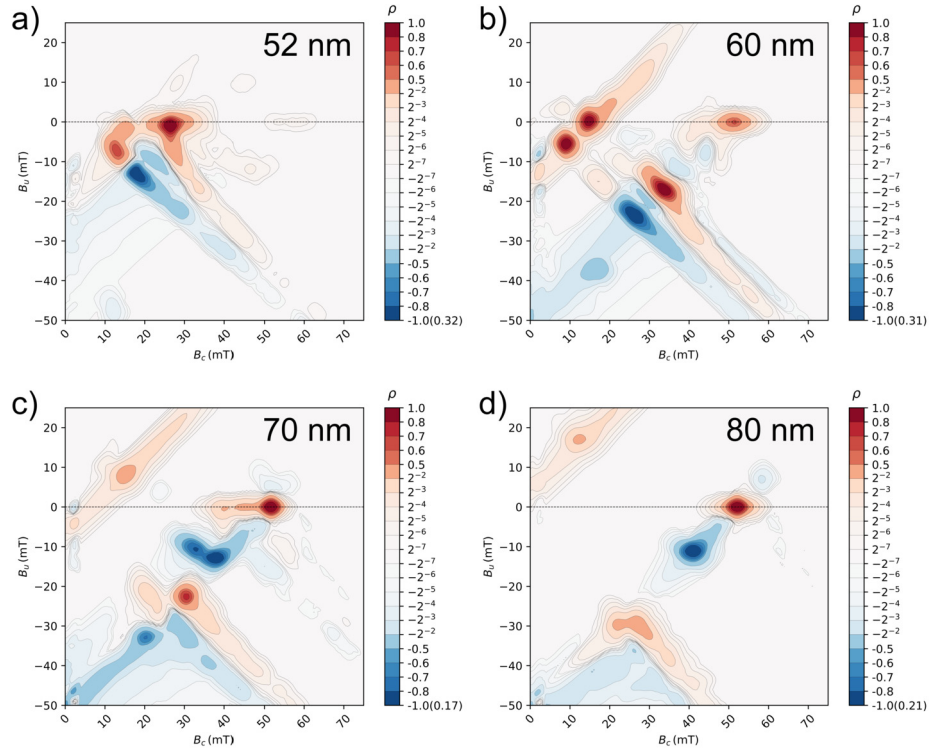
Fig. 4. FORC diagrams with increasing vortex effects. SF = 4 for all diagrams. a) 52 nm; b) 60 nm; c) 66 nm; and d) 76 nm. At these sizes, an ever larger fraction of particle moments begins to switch with nonuniform magnetisations, i.e., vortex nucleation. At 76 nm all particles are in the single vortex remanent state. Dashed contour lines denote negative ρ values. Negative contour values are scaled by the number in brackets at the bottom of the colour-bar legend.
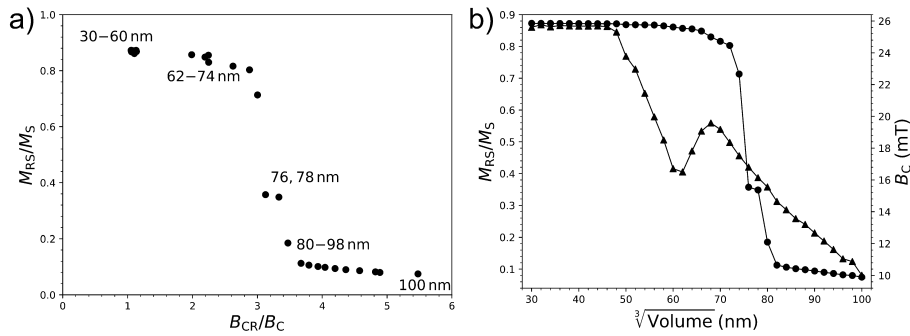

Fig. 5. Day plot and M_{RS}/M_S and coercivity against particle size. a) The Day plot (Day et al., 1977) contains data for SD particles up to 60 nm; however, we know from the micromagnetic solutions that vortices form at sizes from 50 nm upward. Particles with sizes from 62 to 72 nm plot in an unexpected region. Particles larger than 74 nm plot with lower M_{RS}/M_S and higher B_{CR}/B_C values. b) Remanence (circles) and coercivity (triangles) versus particle size.

for $d = 68$ nm. With increasing size, coercivity decreases further, which is accompanied by a sharp M_{RS} decrease (Fig. 5b). The M_{RS} drop is driven by particles nucleating vortices at $B_a > 0$ for $d \geq 68$ nm. For $d \geq 80$ nm, all particles nucleate vortices for $B_a > 0$, thus, the vortex state becomes the remanent magnetic domain state; this is reflected in the Day plot (Day et al., 1977), a plot of the M_{RS}/M_S ratio against the coercivity of remanence B_{CR} (the field necessary to reduce the remanence to zero) to B_C ratio, by the particles 80 nm and larger (Fig. 5a). While it has been argued that the Day plot is ambiguous in many cases (Roberts et al., 2018), the results plotted in Fig. 5a are for calculated responses for particles with known sizes, which is a legitimate use of this type of representation. Particles sized 62–72 nm move away from the top left-hand side of the Day plot (Fig. 5a) to a region with high remanence but larger B_{CR}/B_C values. These sizes coincide with the anomalous coercivity increase for these sizes (Fig. 5b). The increased coercivities can be explained by vortex nucleation, which causes hysteresis loops to become increasingly wasp-waisted (Fig. 6) so that they

cross the zero-magnetisation axis at increasing (absolute) values of the applied field strength. FORC diagrams for these sizes are the most complex of all those simulated here, and have a variety of features (Figs. 4b, 6) caused by the complex interplay of SV and SD effects. The elongated, negative ridge becomes more faint with increasing particle size, whereas the positive responses for $B_u > 0$ become larger and move toward the $B_c = 0$ axis with increasing size (Fig. 4). Positive FORC responses for $B_u > 0$ along the $B_c = 0$ axis are expected for larger multi-domain (MD) grains (Pike et al., 2001; Roberts et al., 2006); it is likely that the tilted positive response with increasing B_u accounts for this.

For the 80 nm particle model, a negative response appears centred roughly at ($B_c = 40$ mT, $B_u = -12$ mT) (Fig. 7, region 5). Fig. 7 represents the contribution of purely SV particles, that is, ensembles of particles that are all in a SV remanent state. It is logical that this FORC diagram is somewhat less complex than those for ensembles with a fraction of particles still in the SD state as well as some in the SV state; the difference is due to the field angle rel-
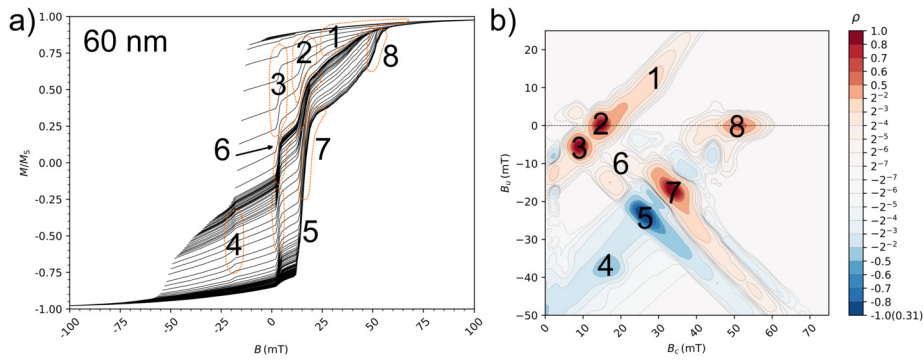
Fig. 6. FORC diagram (SF = 4) (a) and hysteresis curves (b) for 60 nm particles. Annotations link the FORC diagram responses to the raw hysteresis curves. See text for details. Dashed contour lines on the FORC diagram denote negative ρ values. Negative contour values are scaled by the number in brackets at the bottom of the colour-bar legend.
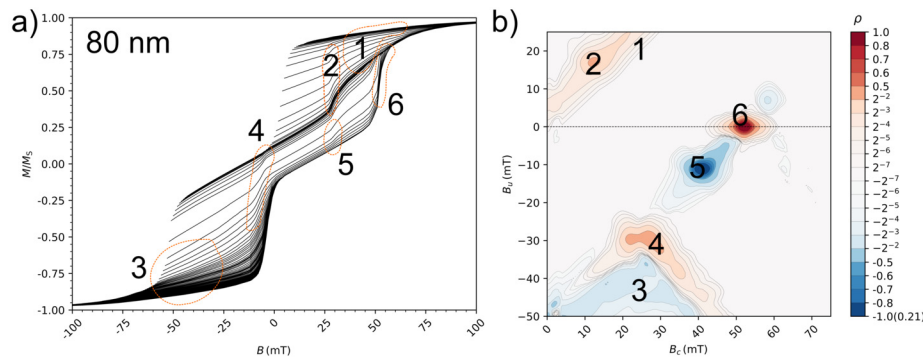
Fig. 7. FORC diagram (SF = 4) (a) and hysteresis curves (b) for 80 nm particles. Annotations link the FORC diagram responses to the raw hysteresis curves. See text for details. Dashed contour lines on the FORC diagram denote negative ρ values. Negative contour values are scaled by the number in brackets at the bottom of the colour-bar legend.
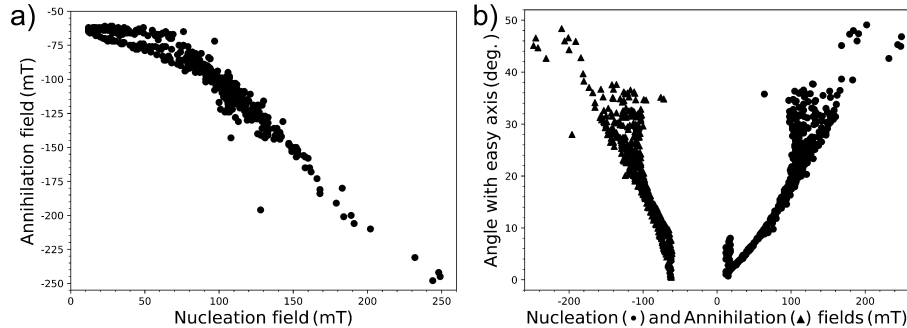
Fig. 8. Vortex nucleation and annihilation fields for the simulated particle ensembles. a) Scatter plot of annihilation field against nucleation field. Three trends are observed depending on whether the nucleated/annihilated vortex has an easy, hard or other alignment. b) Vortex core angle with an easy direction plotted versus the respective nucleation and annihilation fields (circles and triangles, respectively).

ative to particle orientation, as has also been shown by Roberts et al. (2017) for magnetite.

Particles with hard axes aligned closely with the applied field nucleate hard-aligned vortices at high applied field values (Fig. 8); as the field decreases below $\sim$12 mT these vortices rotate irreversibly to an easy axis alignment. As the field is increased on reversal curves with $\sim$0 mT $\leq B_a \leq \sim$ 12 mT these vortices switch irreversibly back to a hard alignment at $B_b \approx 28$ mT to create a local peak at $B_c \approx 12$ mT, $B_u \approx 16$ mT (Fig. 7, region 2); this is manifested in the raw hysteresis data by the smoothed discontinuity at $B \approx 28$ mT whereas the reversible motion traced by the reversal curves around this region accounts for the tilted, elongated response surrounding the local peak (Fig. 7, region 1).

During hysteresis, as the remanent state is approached, all particles ≥ 80 nm have nucleated vortices: particles with easy axis alignment close to the applied field directly nucleate an easy-aligned vortex while the rest nucleate vortices initially oriented

along hard ⟨100⟩ or ⟨110⟩ directions (Fig. 3), which rotate irreversibly to an easy axis alignment as the field approaches zero. The latter fraction of particles then undergoes irreversible rotations back to intermediate positions on FORCs with $\sim$0 mT $\leq B_a \leq$ $\sim$10 mT, at $B_b \approx 4$ mT creating the positive elongated responses (Fig. 7, regions 1, 2).

As the applied field decreases past $\sim$−52 mT, the vortices of particles with easy axis alignment close to the applied field annihilate (Fig. 8). Reversal curves with $\sim$−80 mT $\leq B_a \leq \sim$−52 mT trace lower slopes with decreasing B_a due to the combined reversible motion of vortices and single domains; this is the source of the faint negative contribution for $B_u < \sim$45 mT (Fig. 7, region 3). On increasing B_b on these curves, nucleation of easy-aligned vortices occurs at $\sim$−5 mT creating the boomerang-shaped response (Fig. 7, region 4) that limits the faint negative response in region 3; this corresponds to the smoothed discontinuity in hysteresis curves as the field approaches zero from the left. Increasing the applied field

to positive values causes the easy-aligned vortices of particles with hard axes close to the applied field to switch to hard alignments at ~28 mT, creating a negative FORC region (Fig. 7, region 5). The distribution peak at region 6 (Fig. 7) corresponds to the average annihilation field of vortices on the reversal paths to positive saturation.

There is a large spread in the vortex nucleation and annihilation fields (Fig. 8). Particles with hard axis alignment close to the applied field nucleate hard-aligned vortices for fields as high as ~200 mT and annihilate on the opposite side of the particle for equally high (absolute) values. However, these nucleation and annihilation events make a negligible contribution to the FORC diagram because the change in magnetisation of a particle nucleating/annihilating a hard-aligned vortex from/to a SD state can be as low as 1%.

4. Discussion

Comparison of results for micromagnetic simulations presented here with the coherently rotating dipole model of Valdez-Grijalva and Muxworthy (2018) indicates excellent agreement (Fig. 2). This confirms the accuracy of our model using only 500 random field orientations instead of field orientations on a regular grid, which requires a high density of field orientations near the poles of the sphere. A FORC diagram for SD coherently rotating particles has the same general features as those obtained for weakly interacting SD particles with cubic MCA by Harrison and Lascu (2014), i.e., a positive ridge along the B_c axis, slightly offset toward $B_u < 0$ values and a tilted, negative ridge on the lower half of the FORC plane. For these ensembles, the horizontal spread along the B_c axis corresponds to the density of switching fields of the differently oriented particles and the FORC distribution peak position corresponds directly to the ensemble coercivity. The negative ridge is indicative of intermediate states along the hysteresis curve and, therefore, of SD particles with multi-axial (in this case cubic) MCA types (Valdez-Grijalva and Muxworthy, 2018); this type of FORC response has been identified in simulations for magnetite (Harrison and Lascu, 2014) and hematite (Harrison, 2017), and is potentially unique to non-interacting to weakly interacting SD particles with cubic or other non-uniaxial MCA. Experimental data from the Vulcan iron formation (Michigan, USA) (Laird, 2017) indicates similar FORC diagram patterns for a mixture of SD magnetite and hematite.

The coercivities obtained here are considerably lower than the commonly accepted value for natural greigites of ~60 mT. This discrepancy could be explained by shape anisotropy effects: if the greigite grains are slightly elongated, shape anisotropy can increase the coercive fields, so that the FORC distribution would shift toward higher B_c values. The effect of shape anisotropy would also remove the tilted, negative ridge as no intermediate states along the hysteresis main branch would exist. SD greigite is commonly diagnosed from concentric FORC distributions centred at $B_c \approx 60$ mT (Roberts et al., 2011) without the tilted, negative ridge. Another possibility is for magnetostriction effects to induce a uniaxial anisotropy and increase the coercivities. However, the magnetostrictive properties of greigite are poorly understood.

Whereas the pure SD signal produces a tight, boomerang-shaped FORC distribution (Fig. 2), increasing particle size introduces SV structures that fragment this pattern. The FORC distribution peak is moved toward higher B_c values along the $B_u = 0$ axis. Paradoxically, as this occurs, the bulk coercivity of the ensembles decreases (Fig. 5). This paradox has been observed previously by Dumas et al. (2007) in synthetic size-controlled samples of sub-100 nm Fe dots.

Fragmentation of the FORC diagram for non-uniformly magnetised particles has been observed in experimental studies (Pike and Fernandez, 1999; Dumas et al., 2007; Roberts et al., 2017; Zhao et

al., 2017) and in numerical models (Carvallo et al., 2003; Roberts et al., 2017); however, these studies did not include random field orientation distributions. The trend is, nevertheless, clear and is representative of the complex self-interactions brought about by nonuniform structures and multiple vortex nucleation/annihilation fields (Pike and Fernandez, 1999). It is difficult to compare our results to the FORC signals measured by Muxworthy et al. (2006) and Krása et al. (2011) for synthetic patterned magnetite because many of their FORC diagrams appear to have smoothed the subtle features observed here, which raises questions about the integrity of these samples (e.g., crystallinity) or the adequateness of the FORC measurement density for these samples. However, a general trend is recognised in the elongation of FORC diagram contours in the direction of a negative angle diagonal from the $B_u = 0$ axis. FORC diagrams for coarse-grained synthetic greigite samples (Chang et al., 2007; Roberts et al., 2011) also have this type of elongation as well as a negative ridge probably caused by a fraction of SD particles.

Pike and Fernandez (1999) obtained asymmetric nucleation and annihilation fields of magnetic vortices in nano-patterned Co dots; our models agree with this finding. However, Pike and Fernandez (1999) studied elongated disc-like particles where the vortex cores were always perpendicular to the particle plane that mostly underwent reversible motion from nucleation to annihilation as they traversed the particle. In this study, we demonstrate that different features on SV FORC diagrams are due to a variety of vortex nucleation and annihilation events, which depend on particle alignment with respect to the applied field and on the presence of distinctly different vortex states, i.e., the vortex energies and stabilities depend on their alignment within the crystalline structure (Valdez-Grijalva et al., 2018).

FORC diagrams were averaged for simulations between 30 and 100 nm (Fig. 9a, c) and between 80 and 100 nm (Fig. 9b, d). A normal distribution of sizes with mean $\mu = 50$ nm and standard deviation (s. d.) $\sigma = 16$ nm was used for Figs. 9a, c and a skewed normal distribution of sizes with mean $\mu = 98$ nm and s. d. $\sigma = 8$ mT and skewness parameter $a = -4$ for Figs. 9b, d (our largest simulated particle size being 100 nm requires the skewed distribution because there are no available data beyond this size). The FORC diagram in Fig. 9a has the typical SD pattern surrounded by a variety of more complex responses. This pattern has some similarities to those observed by Dumas et al. (2007) and Muxworthy et al. (2006) for samples that included both SD and SV particles. The FORC distribution peak position no longer coincides with the ensemble coercivity, while still having a response corresponding to the SD fraction.

Both FORC diagrams in Fig. 9 have a significant spread in the positive B_u region. This effect is purely due to domain state and not to magnetostatic interactions. The main peak for these diagrams occurs along the $B_u = 0$ axis at $B_c \approx 52$ mT, which indicates a disconnect with the bulk coercivity of the ensemble. This is a departure from the usual interpretation of FORC diagrams, i.e., that the FORC diagram provides a map of the coercivity distribution. This interpretation holds for SD coherently rotating grains, where the peak response coincides with the value of the ensemble coercivity. It does not hold, however, for SV grains (or for SV-dominated samples) because their coercivity decreases with size while the position of the maximum moves toward higher B_c values. Instead, for SV grains the FORC distribution peak, and most FORC features, should be interpreted as due to vortex nucleation/annihilation fields and their irreversible motions.

5. Conclusions

A micromagnetic FEM/BEM was employed to calculate FORC distributions for non-interacting ensembles of greigite across a size range that spans the SD to SV threshold. 500 random orientations
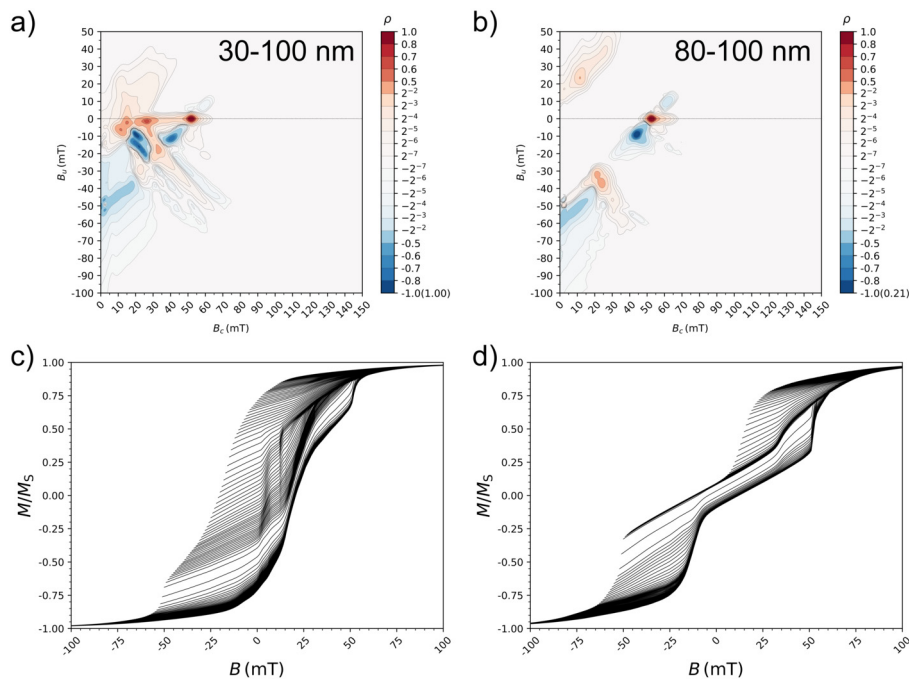
Fig. 9. Averaged FORC diagrams (SF = 4) (top) for multiple particle sizes and corresponding raw hysteresis curves (bottom). Size d distribution of particles a) $30\,nm \le d \le 100\,nm$ and b) $80\,nm \le d \le 100\,nm$ (see text for details). Dashed contour lines denote negative ρ values. Negative contour values are scaled by the number in brackets at the bottom of the colour-bar legend.

from a uniform distribution over a sector of the unit sphere were used for each particle size. This choice was found to be in excellent agreement with previous calculations for SD greigite (Valdez-Grijalva and Muxworthy, 2018).

FORC diagrams are found to be extremely sensitive to the domain state of the simulated particles. When even a small fraction of particles starts to nucleate vortices, e.g., $d \approx 50\,nm$, this is reflected in the FORC diagram (Fig. 4a compared to Fig. 2b). The same cannot be said of the Day plot (Fig. 5a). Anomalous behaviour for particles sized 62 to 72 nm, with coercivity increasing with size was found; these particles plot in an unexpected region of the Day plot. The anomaly disappears for particles > 72 nm, and when $d \ge 76\,nm$ they have much lower M_{RS}/M_S and higher B_{CR}/B_C values.

Detailed FORC analysis and micromagnetic solutions for $d = 80\,nm$ particles reveals the meaning of the FORC diagram for SV ensembles as a map of vortex nucleation/annihilation fields. Interpretation of FORC diagrams as a coercivity distribution does not apply to SV systems (see Pike and Fernandez, 1999; Roberts et al., 2017). Recognition that the remanence in palaeomagnetic studies is often carried by vortex state particles should help users of FORC diagrams to avoid misinterpretation of vertical spread in FORC diagrams, just as it is recognised that vertical spread in MD particles is due to domain wall interactions within particles (Pike et al., 2001). For SD particles, the typical interpretation of the peak position coinciding with the coercivity of the sample holds; however, for SV-dominated samples, the position of the peak occurs at a value much higher than the bulk coercivity of the sample.

The results presented here were obtained for non-interacting greigite particles. Greigite usually occurs as tight clusters where interactions are probably important (Roberts et al., 2011). However, our results have qualitative applicability beyond greigite, for magnetic minerals with cubic MCA such as magnetite and iron, which are known to occur as non-interacting particles. The effects of interparticle magnetostatic interactions within greigite clusters are left for a future study.

References

Almeida, T.P., Kasama, T., Muxworthy, A.R., Williams, W., Nagy, L., Dunin-Borkowski, R.E., 2014. Observing thermomagnetic stability of nonideal magnetite particles: good paleomagnetic recorders? Geophys. Res. Lett. 41 (20), 7041–7047. https://doi.org/10.1002/2014GL061432.

Aragón, R., 1992. Magnetization and exchange in nonstoichiometric magnetite. Phys. Rev. B 46 (9), 5328–5333. https://doi.org/10.1103/PhysRevB.46.5328.

Bloch, F., 1932. Zur theorie des austauschproblems und der remanenzerscheinung der ferromagnetika. In: Zur Theorie des Austauschproblems und der Remanenzerscheinung der Ferromagnetika. Springer, pp. 295–335.

Brown, W.F., 1963. Micromagnetics. Interscience, New York.

Carvallo, C., Muxworthy, A.R., Dunlop, D.J., 2006. First-order reversal curve (FORC) diagrams of magnetic mixtures: micromagnetic models and measurements. Phys. Earth Planet. Inter. 154 (3), 308–322. https://doi.org/10.1016/j.pepi.2005.06.017.

Carvallo, C., Muxworthy, A.R., Dunlop, D.J., Williams, W., 2003. Micromagnetic modeling of first-order reversal curve (FORC) diagrams for single-domain and pseudo-single-domain magnetite. Earth Planet. Sci. Lett. 213 (3), 375–390. https://doi.org/10.1016/S0012-821X(03)00320-0.

Chang, L., Rainford, B.D., Stewart, J.R., Ritter, C., Roberts, A.P., Tang, Y., Chen, Q., 2009. Magnetic structure of greigite (Fe_3S_4) probed by neutron powder diffraction and polarized neutron diffraction. J. Geophys. Res. 114 (B7). https://doi.org/10.1029/2008JB006260.

Chang, L., Roberts, A.P., Muxworthy, A.R., Tang, Y., Chen, Q., Rowan, C.J., Liu, Q., Pruner, P., 2007. Magnetic characteristics of synthetic pseudo-single-domain and multi-domain greigite Fe_3S_4. Geophys. Res. Lett. 34 (24). https://doi.org/10.1029/2007GL032114.

Chang, L., Roberts, A.P., Tang, Y., Rainford, B.D., Muxworthy, A.R., Chen, Q., 2008. Fundamental magnetic parameters from pure synthetic greigite (Fe_3S_4). J. Geophys. Res. 113 (B6). https://doi.org/10.1029/2007JB005502.

Day, R., Fuller, M., Schmidt, V.A., 1977. Hysteresis properties of titanomagnetites: grain-size and compositional dependence. Phys. Earth Planet. Inter. 13 (4), 260–267. https://doi.org/10.1016/0031-9201(77)90108-X.

Dumas, R.K., Li, C.P., Roshchin, I.V., Schuller, I.K., Liu, K., 2007. Magnetic fingerprints of sub-100 nm Fe dots. Phys. Rev. B 75 (13), 134405. https://doi.org/10.1103/PhysRevB.75.134405.

Dunlop, D.J., Özdemir, Ö., 1997. Rock Magnetism. Cambridge University Press, Cambridge.

Egli, R., Chen, A.P., Winklhofer, M., Kodama, K.P., Horng, C.S., 2010. Detection of noninteracting single domain particles using first-order reversal curve diagrams. Geochem. Geophys. Geosyst. 11 (1). https://doi.org/10.1029/2009GC002916.

Fredkin, D.R., Koehler, T.R., 1990. Hybrid method for computing demagnetizing fields. IEEE Trans. Magn. 26 (2), 415–417. https://doi.org/10.1109/20.106342.

Harrison, R.J., 2017. Why do hematite FORCs look weird? In: AGU Fall Meeting. http://adsabs.harvard.edu/abs/2017AGUFMGP23B0924H.

Harrison, R.J., Lascu, I., 2014. Forculator: a micromagnetic tool for simulating first-order reversal curve diagrams. Geochem. Geophys. Geosyst. 15 (12), 4671–4691. https://doi.org/10.1002/2014GC005582.

Kenan, R.P., Glasser, M.L., Milford, F.J., 1963. Spin-wave contribution to the heat capacity of magnetite. Phys. Rev. 132 (1), 47. https://doi.org/10.1103/PhysRev.132.47.

Kouvel, J.S., 1956. Specific heat of a magnetite crystal at liquid helium temperatures. Phys. Rev. 102 (6), 1489. https://doi.org/10.1103/PhysRev.102.1489.

Krása, D., Muxworthy, A.R., Williams, W., 2011. Room- and low-temperature magnetic properties of 2-D magnetite particle arrays. Geophys. J. Int. 185 (1), 167–180. https://doi.org/10.1111/j.1365-246X.2011.04956.x.

Laird, M., 2017. Magnetic Petrophysics of the Vulcan Iron Formation (Michigan, USA). Ph.D. thesis. Michigan Technological University. https://digitalcommons.mtu.edu/etdr/443.

Landau, L.D., Lifshitz, E., 1935. On the theory of the dispersion of magnetic permeability in ferromagnetic bodies. Phys. Z. Sowjetunion 8 (153), 101–114.

Li, G., Zhang, B., Yu, F., Novakova, A.A., Krivenkov, M.S., Kiseleva, T.Y., Chang, L., Rao, J., Polyakov, A.O., Blake, G.R., de Groot, R.A., Palstra, T.T.M., 2014. High-purity Fe$_3$S$_4$ greigite microcrystals for magnetic and electrochemical performance. Chem. Mater. 26 (20), 5821–5829. https://doi.org/10.1021/cm501493m.

Mayergoyz, I., 1986. Mathematical models of hysteresis. IEEE Trans. Magn. 22 (5), 603–608. https://doi.org/10.1109/TMAG.1986.1064347.

Muxworthy, A.R., Heslop, D., Williams, W., 2004. Influence of magnetostatic interactions on first-order-reversal-curve (FORC) diagrams: A micromagnetic approach. Geophys. J. Int. 158 (3), 888–897. https://doi.org/10.1111/j.1365-246X.2004.02358.x.

Muxworthy, A.R., King, J.G., Odling, N., 2006. Magnetic hysteresis properties of interacting and noninteracting micron-sized magnetite produced by electron beam lithography. Geochem. Geophys. Geosyst. 7 (7). https://doi.org/10.1029/2006GC001309.

Muxworthy, A.R., Williams, W., 2005. Magnetostatic interaction fields in first-order-reversal-curve diagrams. J. Appl. Phys. 97 (6), 063905. https://doi.org/10.1063/1.1861518.

Nagy, L., Williams, W., Muxworthy, A.R., Fabian, K., Almeida, T.P., Ó Conbhuí, P., Shcherbakov, V.P., 2017. Stability of equidimensional pseudo-single domain magnetite over billion-year timescales. Proc. Natl. Acad. Sci. USA 114 (39), 10356–10360. https://doi.org/10.1073/pnas.1708344114.

Newell, A.J., 2005. A high-precision model of first-order reversal curve (FORC) functions for single-domain ferromagnets with uniaxial anisotropy. Geochem. Geophys. Geosyst. 6 (5). https://doi.org/10.1029/2004GC000877.

Ó Conbhuí, P., Williams, W., Fabian, K., Ridley, P., Nagy, L., Muxworthy, A.R., 2018. MERRILL: Micromagnetic Earth Related Robust Interpreted Language Laboratory. Geochem. Geophys. Geosyst. 19 (4), 1080–1106. https://doi.org/10.1002/2017GC007279.

Pike, C., Fernandez, A., 1999. An investigation of magnetic reversal in submicron-scale Co dots using first order reversal curve diagrams. J. Appl. Phys. 85 (9), 6668–6676. https://doi.org/10.1063/1.370177.

Pike, C.R., Roberts, A.P., Dekkers, M.J., Verosub, K.L., 2001. An investigation of multi-domain hysteresis mechanisms using FORC diagrams. Phys. Earth Planet. Inter. 126 (1), 11–25. https://doi.org/10.1016/S0031-9201(01)00241-2.

Pike, C.R., Roberts, A.P., Verosub, K.L., 1999. Characterizing interactions in fine magnetic particle systems using first order reversal curves. J. Appl. Phys. 85 (9), 6660–6667. https://doi.org/10.1063/1.370176.

Rave, W., Ramstöck, K., Hubert, A., 1998. Corners and nucleation in micromagnetics. J. Magn. Magn. Mater. 183 (3), 329–333. https://doi.org/10.1016/S0304-8853(97)01086-X.

Roberts, A.P., 2015. Magnetic mineral diagenesis. Earth-Sci. Rev. 151, 1–47. https://doi.org/10.1016/j.earscirev.2015.09.010.

Roberts, A.P., Almeida, T.P., Church, N.S., Harrison, R.J., Helsop, D., Li, Y., Li, J., Muxworthy, A.R., Williams, W., Zhao, X., 2017. Resolving the origin of pseudo-single domain magnetic behavior. J. Geophys. Res. 122 (12), 9534–9558. https://doi.org/10.1002/2017JB014860.

Roberts, A.P., Chang, L., Rowan, C.J., Horng, C.S., Florindo, F., 2011. Magnetic properties of sedimentary greigite (Fe$_3$S$_4$): an update. Rev. Geophys. 49 (1). https://doi.org/10.1029/2010RG000336.

Roberts, A.P., Heslop, D., Zhao, X., Pike, C.R., 2014. Understanding fine magnetic particle systems through use of first-order reversal curve diagrams. Rev. Geophys. 52 (4), 557–602. https://doi.org/10.1002/2014RG000462.

Roberts, A.P., Liu, Q., Rowan, C.J., Chang, L., Carvallo, C., Torrent, J., Horng, C.S., 2006. Characterization of hematite (α-Fe$_2$O$_3$), goethite (α-FeOOH), greigite (Fe$_3$S$_4$), and pyrrhotite (Fe$_7$S$_8$) using first-order reversal curve diagrams. J. Geophys. Res. 111 (B12). https://doi.org/10.1029/2006JB004715.

Roberts, A.P., Pike, C.R., Verosub, K.L., 2000. First-order reversal curve diagrams: a new tool for characterizing the magnetic properties of natural samples. J. Geophys. Res. 105 (B12), 28461–28475. https://doi.org/10.1029/2000JB900326.

Roberts, A.P., Tauxe, L., Heslop, D., Zhao, X., Jiang, Z., 2018. A critical appraisal of the "Day diagram". J. Geophys. Res. 123 (4), 2618–2644. https://doi.org/10.1002/2017JB015247.

Snowball, I.F., 1997. Gyroremanent magnetization and the magnetic properties of greigite-bearing clays in southern Sweden. Geophys. J. Int. 129 (3), 624–636. https://doi.org/10.1111/j.1365-246X.1997.tb04498.x.

Torrie, B.H., 1967. Spin waves in magnetite at a temperature below the electronic ordering transition. Solid State Commun. 5 (9), 715–717. https://doi.org/10.1016/0038-1098(67)90356-0.

Valdez-Grijalva, M.A., Muxworthy, A.R., 2018. First-order reversal curve (FORC) diagrams of nanomagnets with cubic magnetocrystalline anisotropy: A numerical approach. J. Magn. Magn. Mater. Submitted for publication.

Valdez-Grijalva, M.A., Nagy, L., Muxworthy, A.R., Williams, W., Fabian, K., 2018. The magnetic structure and palaeomagnetic recording fidelity of sub-micron greigite (Fe$_3$S$_4$). Earth Planet. Sci. Lett. 483, 76–89. https://doi.org/10.1016/j.epsl.2017.12.015.

Vasiliev, I., Franke, C., Meeldijk, J.D., Dekkers, M.J., Langereis, C.G., Krigjsman, W., 2008. Putative greigite magnetofossils from the Pliocene epoch. Nat. Geosci. 1 (11), 782–786. https://doi.org/10.1038/ngeo335.

Winklhofer, M., Chang, L., Eder, S.H.K., 2014. On the magnetocrystalline anisotropy of greigite (Fe$_3$S$_4$). Geochem. Geophys. Geosyst. 15 (4), 1558–1579. https://doi.org/10.1002/2013GC005121.

Zhao, X., Roberts, A.P., Heslop, D., Paterson, G.A., Li, Y., Li, J., 2017. Magnetic domain state diagnosis using hysteresis reversal curves. J. Geophys. Res. 122 (7), 4767–4789. https://doi.org/10.1002/2016JB013683.